https://doi.org/10.5194/egusphere-2026-2931
Preprint. Discussion started: 4 June 2026

Electrostatics and Collision Dynamics of Ice and Anthropogenic Smoke Particles in the Mesosphere/Lower Thermosphere

Trinesh Sana[1], Sanjay K. Mishra[1], and Ingrid Mann[2]
[1]Planetary Sciences Division, Physical Research Laboratory, Ahmedabad, India
[2]Department of Physics and Technology, UiT The Arctic University of Norway, Tromsø, Norway
Correspondence: Trinesh Sana (sanatrinesh@gmail.com) and Ingrid Mann (ingrid.b.mann@uit.no)

Abstract. The increase in satellite launches raises the anthropogenic influx of various elements into the Mesosphere and Lower Thermosphere (MLT), comparable to the natural influx caused by meteoric ablation. This study investigates the electrostatic interactions between ice particles and remnants of space debris using a classical electrostatic framework. Aside from the Coulomb interaction, the attractive force between two particles at short distances, arising from polarization, is taken into account. Collision outcomes, the effective velocity regime for collisions, and the subsequent aggregation probability are estimated. Aggregation is limited to a specific range of collision velocities between minimum and maximum values. This range varies depending on factors such as particle size, mass density, and dielectric constant. For most particles, the aggregation velocities range from a few m s^{-1} to several tens of m s^{-1}, where smaller particles may need significantly higher velocities to form stable aggregates. When considering the collisions of particles in thermal motion, it is found that Al_2O_3 (due to its greater abundance) and TiO_2 (due to its higher dielectric constant), both originating from anthropogenic sources, may dominate in the formation of ice-anthropogenic particle aggregates. In the MLT region, the formation of stable aggregates from the collision of ice with particles from space debris, which one may denote as anthropogenic smoke particles (ASPs), is similar to that from collisions with meteoric smoke particles (MSPs).

1 Introduction

Due to the increasing number of space program projects, perhaps 75,000 additional satellites will be in orbit by 2030 (Schulz and Glassmeier, 2021; Howard and Ah, 2022; Murphy et al., 2023; Schulz et al., 2026). Defunct satellites, spent rocket stages, fragmentation events, and mission-related ejecta lead to the rapid accumulation of anthropogenic space debris. They pose a major concern for both spacecraft safety and the long-term sustainability of the near-Earth space environment. These pieces of space debris re-enter the Earth's upper atmosphere, along with the natural influx from meteoroids, undergo intense aerodynamic heating, ablation, and fragmentation, and inject metal atoms to form metal layers (Schulz and Glassmeier, 2021).

The space debris is composed of many elements, particularly Li, Al, Cu, Nb, Hf, Pb, Be, Mg, Ti, Cr, Fe, Ni, Zr, Ga, Mo, In, Sn, Ba, Ce, Ta, W, Sb, Bi, Cd, Pr, and Nd (Murphy et al., 2023; Schulz and Glassmeier, 2021; Schulz et al., 2026). Schulz and Glassmeier (2021) reported anthropogenic materials contribute about 2.8% compared to the annual influx of interplanetary dust particles. They further suggested that atmospheric re-entry of space debris may increase by 13% to 40% in the near future.

Recently, Schulz et al. (2026) updated the estimates of annual anthropogenic influx into the Earth's atmosphere. Confirming the findings from the earlier work, they further report that the injected mass doubled between 2020 and 2024, reaching 887±123 tonnes in 2024. This results in a 16% increase in anthropogenic metal injection into the mesosphere/lower thermosphere (MLT) region (between 70 to 120 km) compared to the natural meteoric metal injection as of 2024 (Schulz et al., 2026). It is anticipated that, in the future, over 75,000 large constellation satellites could increase this value to 70% (Schulz et al., 2026). As a result, the mass influx of elements from space debris is becoming significant and comparable to the natural input by meteoroid ablation. Additionally, some metals, such as Al and Cu, are dominantly originating from human space activities. In a 75,000-satellite constellation future scenario, Schulz et al. (2026) predicted that the annual elemental mass injection for Al and Ti will be increased by factors of 13.1 ± 4.4 and 22.9 ± 7.6 respectively. The detailed estimates for other elements are given in Table 5 of Schulz et al. (2026). Thus, space debris may significantly influence the formation of high-altitude clouds, introduce new chemical pathways, affect radiative forcing, and produce particles with unique optical properties (Murphy et al., 2023; Schulz et al., 2026).

In the MLT region, the presence of highly reactive atomic oxygen leads to the formation of metal oxides, which later form nm-sized meteoric smoke particles (MSPs) (Plane, 2003). The interactions and growth of solid particles in the MLT have been studied in detail for MSPs, focusing on their transport and growth (Megner et al., 2008; Bardeen et al., 2008), their influence on the charge balance (Baumann et al., 2013, 2015), and their origin from meteors (Plane et al., 2015). Additionally, there is evidence that charged MSPs influence the radar diagnostics of the D-region ionosphere using incoherent scatter (Gunnarsdottir et al., 2024). Charged MSPs may interact electrostatically, influencing the chemical and microphysical framework of the MLT through processes such as electron depletion, ion balance modification, and ice-particle coagulation (Baumann et al., 2015). These MSPs may also act as condensation nuclei for heterogeneous ice particle formation. In the Polar Region, during the summer, due to summer-to-winter meridional circulation, air experiences adiabatic cooling in the mesosphere, causing temperatures to drop significantly to around 120 K. The low temperatures, combined with atmospheric water, allow ice particles to form. During polar summer, the aggregation of the ice particles forms polar mesospheric clouds, which give rise to noctilucent clouds (NLC) observed from the ground and contribute to the formation of radar echoes known as polar mesospheric summer echoes. Both phenomena, which are observed from the Earth, have increased in recent years (Latteck et al., 2021). The increase in water in the MLT is likely a decisive factor for this (Lübken et al., 2021), while studies on ice formation indicate that the formation of ice particles must occur through heterogeneous condensation (Tanaka et al., 2022). These are of considerable interest on account of their potential relevance to global warming. Therefore, the influence of anthropogenically originated particles on the formation of NLC is possibly significant, and it is crucial to thoroughly investigate their role in the growth process. The formation process of these particles is poorly constrained. Due to their similarity with MSPs, we refer to these particles as anthropogenic smoke particles (ASPs).

In the MLT region, which consists of a weakly ionized, complex dusty plasma, the space debris, MSPs, and ice particles become electrically charged through mechanisms such as electron and ion accretion, photoemission, and other ionization processes (Rapp and Thomas, 2006; Mann et al., 2014). The description of the interactions is largely based on theoretical considerations, the physical properties depend on the dust composition, and in addition, small size effects become important for

https://doi.org/10.5194/egusphere-2026-2931
Preprint. Discussion started: 4 June 2026

particle sizes of a few nm (Mann et al., 2014). As the surface charge on the particles significantly influences their agglomeration, it should be considered to investigate the growth of ice onto the ASPs, and electrostatic interactions should be taken into account. Given that the frequency of ice particles in the MLT appears to have increased in recent decades, it is reasonable to investigate the extent to which anthropogenic particles contribute to this increase.

In this paper, we investigate electrostatic interactions between charged ice and a component of the solid particles predicted to form from space debris, that is, the ASP. The study by Baptiste et al. (2021) demonstrated how electrostatic interactions influence the growth of MSPs and ice particles, but did not take into account space debris particles. The model of Bichoutskaia et al. (2010) has been applied to quantify the electrostatic interaction energy between charged ice and oxides. Due to its dielectric nature, two particles with charges of the same sign can experience a strong attractive interaction at small separation distances. This attractive interaction is determined by the polarization of surface charge, resulting in regions of positive and negative surface charge density on one particle due to the other. Therefore, the collision outcomes and the subsequent formation of a stable aggregate differ significantly among oppositely charged, likely charged, and charge-neutral particle collisions.

The remainder of this manuscript is organized as follows: Section 2 outlines the applied model framework of electrostatics and collisions, along with the parameters assumed for particles in the MLT. Section 3 presents the numerical results, and Section 4 provides a concluding discussion. Additionally, Appendix A & B contain a series of tables summarizing the numerical results obtained.

2 Electrostatics and Collision Dynamics

The MLT region constitutes a weakly ionized dusty plasma environment composed of electrons, positive ions, neutral species (Mann et al., 2019). At MLT altitudes, the temperature is extremely low (110–150 K). The ambient plasma density varies strongly between day and night conditions, with typical electron densities ranging from ~ 35 cm^{-3} at night to $\sim 4.5 \times 10^3$ cm^{-3} during daytime conditions (Havnes et al., 2001; Sodha et al., 2011). The ice, ASPs, and MSPs are embedded within this plasma medium. They undergo electrostatic charging via electron and ion collection currents at the particle surface. Further, under the exposure to extreme EUV/UV fluxes, photoelectrons are also emitted from the ice and dust particles. However, the degree of photoemission is significantly dependent on the work function of the particles. The work function of ice varies in a wide range, from as high as 8.7 eV for pure ice to as low as 2.3 eV for dirty ice (Misra et al., 2011). Since the dust number density is comparable to that of ambient plasma electrons and ions, we can estimate the dust charge by examining the collective variation in plasma electron and ion densities. This assessment should consider the effects of plasma particle capture, photodetachment, and photoionization (Sodha et al., 2011; Misra et al., 2011; Baumann et al., 2013, 2015). For mesospheric ice particles and MSPs, the typical charge state varies around $(0, -1e, -2e)$ (Sodha et al., 2011). Since the dust/ice charging is independent of the origin of the particles in the MLT region, the charge state of ASPs will vary similarly to that of MSPs. Overall, the mesospheric ice and dust particles in the MLT usually have a charge of $-1e$. And a large fraction of nanometer-sized dust particles also remains neutral. Depending on mechanisms such as electron bite-out or dominant photoemission from dirty ice, ice and dust particles may also acquire positive charges.

Table 1. Dielectric constants and mass densities of ice and metal oxides considered in this study

Particle	Dielectric constant	Density (g/cc)
Ice, H2O	100	0.92
Iron oxide, FeO	14.2	5.74
Silicon dioxide, SiO2	3.9	2.65
Aluminium oxide, Al2O3	9	3.50
Titanium dioxide, TiO2	95	4.25
Magnesium oxide, MgO	9.6	3.58

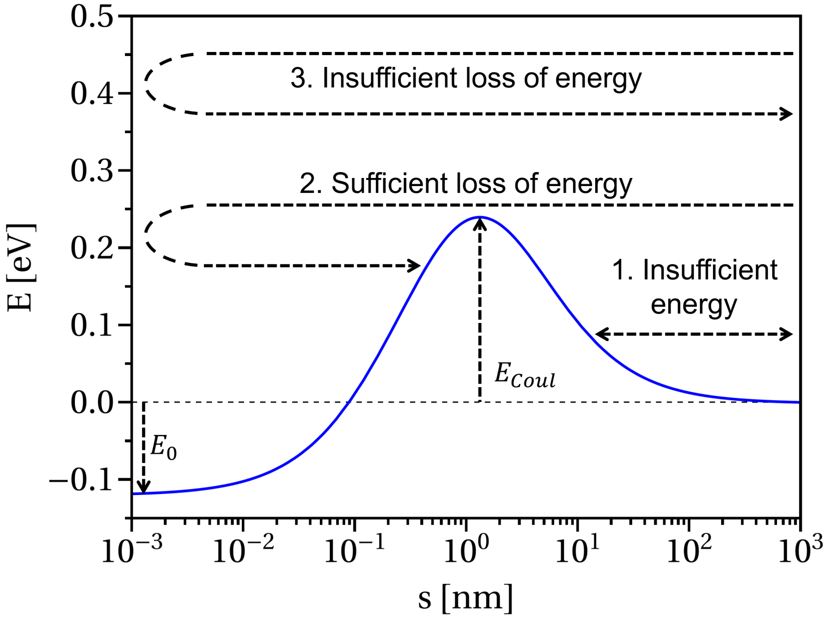

Figure 1. Illustration of the electrostatic interaction energy between a singly negatively charged ice particle ($r_{H_2O} = 1$ nm) and a singly negatively charged SiO_2 particle ($r_{SiO_2} = 0.2$ nm) for varying separations derived using the model of Bichoutskaia et al. (2010).

Apart from the surface charge, the electrostatic interactions between charged spherical ice particles and oxides depend on their particle size and dielectric constants. To investigate the electrostatics, collision dynamics, and coalescence of ice and space debris, we consider charged ice particles with radii ranging from 1 to 100 nm and various oxides with radii ranging from 1 to 5 nm. Aluminum being the most dominant, Al_2O_3 has been selected for this study. TiO_2 has been selected for its very high dielectric constant compared to other compounds found in space debris. We also select three other oxides, FeO, MgO, and SiO_2, because Fe, Mg, and Si are the next most common elements in space debris. However, these three elements are also dominant in sources from natural influx. Note that the study of all individual oxides is computationally expensive, so we restrict our study to these five oxides. To study particle growth, collision outcomes, and the subsequent formation of a stable aggregate, it is necessary to consider the surface charges, dielectric constants, and mass densities of the two colliding particles. The dielectric constants and mass densities are given in Table 1. The selected parametric regime in this study encompasses the dielectric constants and mass densities expected for various oxides related to space debris. Figure 1 shows an example of an electrostatic interaction energy curve between like-charged spherical ice and SiO_2. The distinct features are: i) at large separations, there is no interaction. ii) As the separation decreases to a certain amount, they will feel a repulsive Coulomb barrier (hill) (E_{Coul}). iii) At a very small separation (which may be considered as the point of contact), the electrostatic energy becomes negative $(E_0 < 0)$. E_0 can be considered as the binding energy. Note that, depending on the particle sizes and dielectric constants, E_0 can be negative, positive, or zero, but always less than or equal to the Coulomb barrier, i.e., $E_{Coul} \geq E_0$. Because at a small separation, the polarization effect of one particle on the other reduces the repulsion by inducing opposite surface charge. For a system with one charged particle and another neutral, the Coulomb barrier is absent, $E_{Coul} = 0$, and an attractive well will be created between infinity with zero energy and at the point of contact with $E_0 < 0$.

The electrostatic interaction energy plays a crucial role in determining the outcome of particle collisions. It determines the effective velocity regime for the formation of a stable aggregate following a collision. Based on the Figure 1, during a collision event between two like-charged particles, the particles have to overcome the Columb hill (E_{Coul}). So, the relative kinetic energy with respect to the center of mass must be higher than E_{Coul}. Therefore, the minimum relative initial velocity of the colliding particles required to overcome the Coulomb barrier is

$$u_{\text{min}} = \sqrt{\frac{2eE_{Coul}}{\mu}}\,, \tag{1}$$

where $\mu = \frac{m_{H_2O} m_{\text{Oxide}}}{m_{H_2O} + m_{\text{Oxide}}}$ is the reduced mass of the colliding ice (with mass m_{H_2O}) and oxides (with mass m_{Oxide}), and e is the electronic charge. After overcoming the Coulomb hill, the collision occurs. The kinetic energy just before the collision is

$$\text{KE}_{\text{Before}} = \frac{1}{2}\mu u^2 - eE_0\,. \tag{2}$$

After the collision, the energy is reduced by

$$\text{KE}_{\text{After}} = k_r^2 \times \text{KE}_{\text{Before}}\,, \tag{3}$$

where k_r is the coefficient of restitution. Following Baptiste et al. (2021), we have taken $k_r = 0.9$ in this study. If this excess energy $\mathrm{KE}_{\mathrm{After}}$ is less than the barrier $E_{Coul} - E_0$, then coalescence is possible. Otherwise, the particles will move apart after the collision. Hence, the maximum velocity beyond which coalescence is not possible can be derived as

$$\mathrm{KE}_{\mathrm{After}} = k_r^2 \times \mathrm{KE}_{\mathrm{Before}} = e(E_{Coul} - E_0), \tag{4}$$

or

$$u_{\max} = \sqrt{\frac{2e\left[(E_{Coul} - E_0)/k_r^2 + E_0\right]}{\mu}}. \tag{5}$$

Therefore, particles with relative velocities between $(u_{\min}, u_{\max})$ can form stable aggregates after collision. In the case of a collision between charged-neutral and oppositely charged particles, the minimum speed becomes zero.

Note that the aggregation of FeO, MgO, and SiO_2 with H_2O ice has been discussed earlier by Baptiste et al. (2021). They highlighted that the specific location of the point charge on the particle's surface can influence the electrostatic interaction between two like-charged particles. This influence is significant for sub-nanometer-sized particles. For particle sizes of $r_{\mathrm{Oxide}} \geq 1$ nm, we observe that the difference between the model outcomes of aggregation probability of Baptiste et al. (2021) and Bichoutskaia et al. (2010) is only about 5% in the case of H_2O ice and metal oxide aggregation. Baptiste et al. (2021) conducted their analysis of the aggregation of like-charged FeO and MgO with ice up to $r_{H_2O} = 30$ nm. In the present study, we are extending this analysis to $r_{H_2O} = 100$ nm. Additionally, we have further examined the outcomes of collisions in scenarios involving charged ice and neutral oxide aggregation.

3 Numerical Results

The framework presented in Bichoutskaia et al. (2010) has been utilized to derive the electrostatic interaction energy between charged ice and various oxides. The basic equations to derive E_{Coul} and E_0 have been solved using the method explained in Brazil Lindgren (2017). Thereafter $u_{\min}$ and $u_{\max}$ have been derived using Eqs. (1) and (5). Figure 2 illustrates the variation $u_{\min}$ (blue) and $u_{\max}$ (red) derived from the electrostatic interaction energy between a singly negatively charged ice particle and a singly negatively charged metal oxide. The variation of relative thermal speed $u_{th} = \left(2k_B T/\mu\right)^{1/2}$ (green) is also shown for different r_{H_2O} and r_{Oxide}. In the mesospheric condition, T is taken to be 150 K following Baptiste et al. (2021). As $u_{\min}$, $u_{\max}$, and u_{th} are inversely proportional to the square root of the reduced mass of the system, i.e., $\left(\propto 1/\sqrt{\mu}\right)$, and larger particles have higher masses, these velocities reduce with increasing radius of the ice and oxide particles. The estimated $(u_{\min}, u_{\max})$ are around ∼ (250, 250) m s^{-1} and ∼ (110, 125) m s^{-1} for ($r_{H_2O} = 1$ nm, $r_{\mathrm{Oxide}} = 1$ nm) and ($r_{H_2O} = 1$ nm, $r_{\mathrm{Oxide}} = 5$ nm) respectively. While increasing the r_{H_2O} to 100 nm, the velocity range decreases to ∼ (10, 40) m s^{-1} and ∼ (1, 2) m s^{-1} for $r_{\mathrm{Oxide}} = 1$ nm and $r_{\mathrm{Oxide}} = 5$ nm, respectively. The detailed quantitative estimates of $(u_{\min}, u_{\max})$ for different like-charged ice-ASP collisions are given in the Tables of Appendix A. It is further observed that the velocity interval, i.e., $u_{\max} - u_{\min}$,

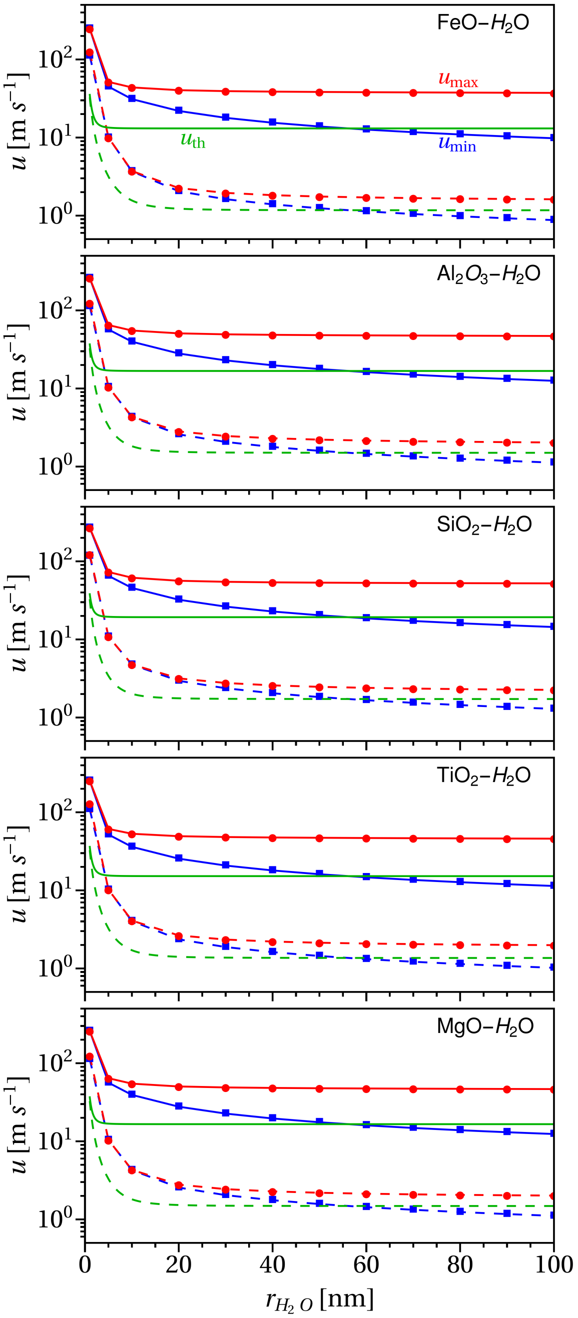

Figure 2. Variation of u_{min} (blue), u_{max} (red), and $u_{th} = \left(2k_BT/\mu\right)^{1/2}$ (green) as a function of r_{H_2O}, needed for collision between ice and various metal oxides. The solid and dashed lines are for $r_{\text{Oxide}} = 1$ nm and 5 nm, respectively. The colors are explained in the uppermost panel. Other parameter used: $q_{H_2O} = q_{\text{Oxide}} = -1e$.

increases with increasing r_{H_2O} for $r_{H_2O} \geq r_{\text{Oxide}}$. This can be attributed to the fact that charged smaller ice particles create significantly more Coulomb repulsion than the induced polarization effect on like-charged ASPs, due to their smaller available area for polarization. This results in $|E_{Coul}| \geq |E_0|$ and E_{Coul} dominates in the estimates of $(u_{\text{min}}, u_{\text{max}})$ for smaller $r_{H_2O} \leq 10$ nm. Here $|a|$ represents the magnitude of a. On the contrary, a higher polarization effect is created for larger r_{H_2O} leading to $|E_0| \geq |E_{Coul}|$, which makes E_0 dominate in u_{max}. Furthermore, the estimated u_{min} and u_{max} for $r_{H_2O} \lesssim 55$ nm, are larger than the characteristic u_{th} of the particle population. This implies that the collision velocities exceeding the thermal regime are physically accessible for the growth process. However, for $r_{H_2O} \gtrsim 55$ nm, the thermal population can contribute to the aggregation process due to $u_{\text{min}} \leq u_{th} < u_{\text{max}}$.

TiO_2 and SiO_2 exhibit the lowest and highest E_{Coul} values, respectively, because of their higher and lower dielectric constants, which influence the polarization effect. Additionally, at low density, SiO_2 has higher values of u_{min} and u_{max} (as shown in the third panel in Figure 2). On the contrary, FeO with a higher density has the lowest values of u_{min} and u_{max} (as shown in the top panel in Figure 2). Whereas with a higher dielectric constant but lower density, TiO_2 has the next lowest values of u_{min} and u_{max} (as shown in the fourth panel from the top in Figure 2). Lastly, with comparable values of dielectric constant and density, the u_{min} and u_{max} values are observed to be similar for Al_2O_3 and MgO (as shown in the second and fifth panels from the top in Figure 2). For the case of fixed singly negative charge ice and oxides with ($r_{H_2O} = 1$ nm, $r_{\text{Oxide}} = 1$ nm) and ($r_{H_2O} = 5$ nm, $r_{\text{Oxide}} = 5$ nm), we observed that $E_{Coul} \approx E_0$ for all the metal oxides. For these cases, the polarization effect is not strong enough to create the attractive energy well. Aggregation is not possible in these cases.

The u_{max} for the case of charged ice and neutral metal oxide aggregation is shown in Figure 3. In this case, u_{max} decreases approximately three orders of magnitude within $r_{H_2O} = 20$ nm. Note that the charged ice particle induces polarization on the neutral oxides. The degree of polarization depends on the surface charge density on the ice. For a singly charged ice, the surface charge density decreases as $\propto 1/r^2_{H_2O}$, leading to a rapid decrease of E_0 in magnitude. This results in a decrease in u_{max} with increase in r_{H_2O}. For smaller values of $r_{H_2O} < 5$ nm, we observe an increase in u_{max} with increase in r_{Oxide}. An increase in r_{Oxide} increases the effective area on the neutral oxides, which results in a higher area available for polarization, leading to an increase in E_0 and subsequently u_{max}. However, for $r_{H_2O} \geq 5$ nm, a slight decrease in u_{max} is observed for larger r_{Oxide}. This can be attributed to a smaller degree of polarization from larger ice particles to relatively heavier oxides, effectively lowering u_{max}. TiO_2 with the highest dielectric constant among the oxides used in this study exhibits the highest u_{max} due to a higher degree of polarization. For smaller values of r_{H_2O}, SiO_2, with the lowest value of dielectric constant, leads to the lowest u_{max} values. However, FeO has the lowest u_{max} for higher r_{H_2O} due to its higher mass density. Overall, u_{max} ranges from few tens of m s^{-1} for $r_{H_2O} < 5$ nm to few times of 0.1 m s^{-1} for $r_{H_2O} \geq 5$ nm. The detailed quantitative estimates of u_{max} for different charged-neutral ice-ASP collisions are given in the Tables of Appendix B.

3.1 Aggregation probability

Based on the estimated effective relative velocity between oxides (of anthropogenic origin) and ice particles, we can establish initial constraints on the likelihood of aggregation in the MLT region. However, the actual velocity distribution of these anthropogenic particulates in the MLT region is presently unknown. The velocity regime may depend on the deceleration histories

https://doi.org/10.5194/egusphere-2026-2931
Preprint. Discussion started: 4 June 2026

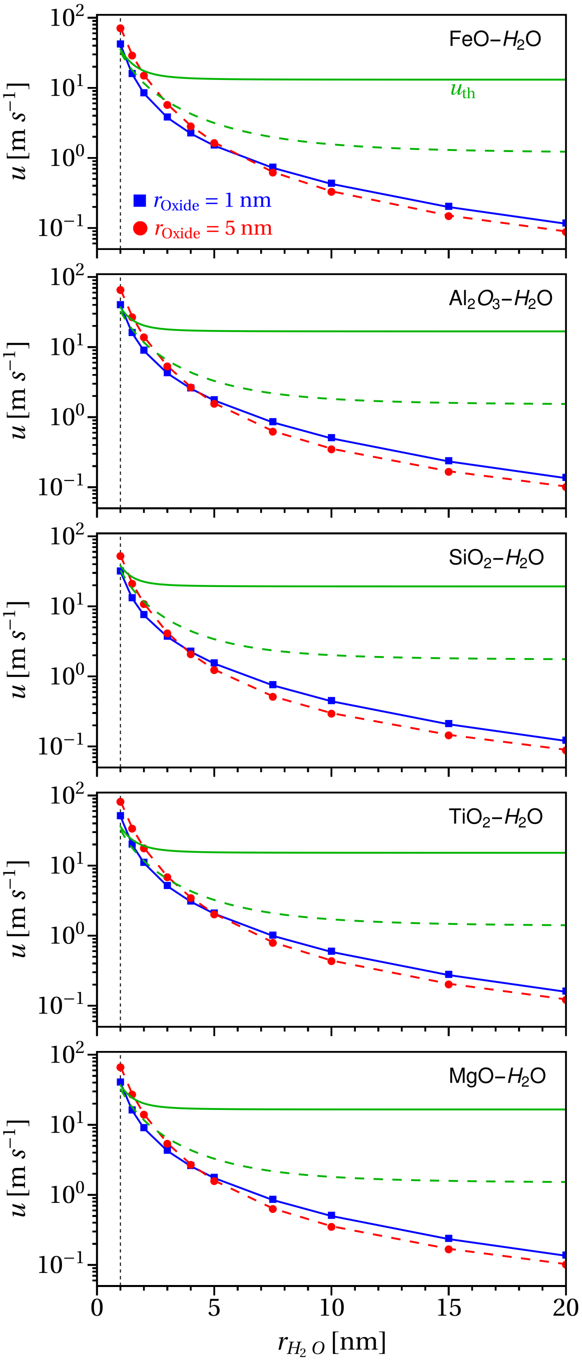

Figure 3. Variation of $u_{\max}$ and u_{th} (green) as a function of r_{H_2O} needed for collision between charged ice and various neutral metal oxides. The solid and dashed lines are for $r_{\text{Oxide}} = 1$ nm (blue) and 5 nm (red), respectively. The colors are explained in the uppermost panel. Other parameter used: $q_{H_2O} = -1e$, $q_{\text{Oxide}} = 0$.

and processes during re-entry to the MLT. If the particles are moving at a roughly constant speed within the range of (u_{min}, u_{max}), the aggregation probability will be 100%. However, for a first-order approximation, assuming these debris behave similarly to naturally generated MSPs, the effective velocity distribution may be represented by a Maxwell-Boltzmann distribution in the MLT temperature regime. Following Baptiste et al. (2021), the distribution can be written as

$$f(u) = \sqrt{\frac{2}{\pi}} \left(\frac{\mu}{k_B T}\right)^{3/2} u^2 \exp\left(-\frac{\mu u^2}{2k_B T}\right), \tag{6}$$

where k_B is the Boltzmann constant and T is the temperature in the MLT region. Then the aggregation probability can be written as:

$$\text{Agg. probability } [\%] = \int\limits_{u_{\text{min}}}^{u_{\text{max}}} f(u)du\,. \tag{7}$$

It is observed from Figure 2 that for the like-charged ice-oxide aggregation case, for $r_{H_2O} \lesssim 55$ nm, u_{min} and u_{max} remain greater than u_{th}, suggesting only the high-energy Maxwellian tail of the distribution forms stable aggregates after collision. For $r_{H_2O} \gtrsim 55$ nm, u_{min} becomes lower than u_{th}, indicating that a significant fraction of particles near the Maxwellian peak can actively participate in the collision process. Figure 4 illustrates the aggregation probability for like-charged ice-oxide collision, where r_{H_2O} increased to 100 nm for fixed $r_{\text{Oxide}} = 1$ (blue) and 5 (red) nm. Similar to Baptiste et al. (2021), we also observed a one order of magnitude increase in the aggregation probability with an increase in r_{H_2O} from 10 to 100 nm. Our further observations revealed no significant differences in the aggregation probability profile across different ice-oxide aggregations. Figure 4 also highlights that the maximum aggregation probability decreases from 77% to approximately 50% upon an increase in $r_{\text{Oxide}} = 1$ (blue) to 5 (red) nm for $r_{H_2O} = 100$ nm due to the increase in m_{Oxide}.

The aggregation probability for charged ice-neutral oxide collision has been shown in Figure 5. For smaller r_{H_2O}, Figure 3 shows that $u_{\text{max}} \geq u_{th}$, which leads to greater coverage of the Maxwell-Boltzmann distribution. However, a higher r_{H_2O} results in a significantly smaller u_{max} compared to u_{th}, indicating that particles with high speed move apart after a collision. This results in a decrease in aggregation probability with increasing r_{H_2O}. For $r_{\text{Oxide}} = 1$ and 5 nm, approximately seven and four orders of magnitude decrease is observed, respectively, while increasing r_{H_2O} from 1 to 20 nm. TiO_2 and SiO_2 exhibit the highest and lowest aggregation probability, respectively, because of their higher and lower dielectric constants. The probability of aggregation increases with the dielectric constants and radius of oxides due to the enhanced strength and effective area of the polarization effect, respectively. Overall, the collision outcome between ASPs and mesospheric ice particles depends on their sizes, dielectric constants, and mass densities. The models of electrostatic interaction are independent of the origin of the ASPs or MSPs. Hence, ASPs exhibit aggregation behavior similar to that of the ice-MSP aggregation regime reported by Baptiste et al. (2021). The aggregation further depends on the concentrations of specific elements in the MLT region, along with the other parameters discussed above. The observed agreement suggests that this distinct anthropogenic particle population can be detected and systematically studied within the well-established naturally originated MSP framework.

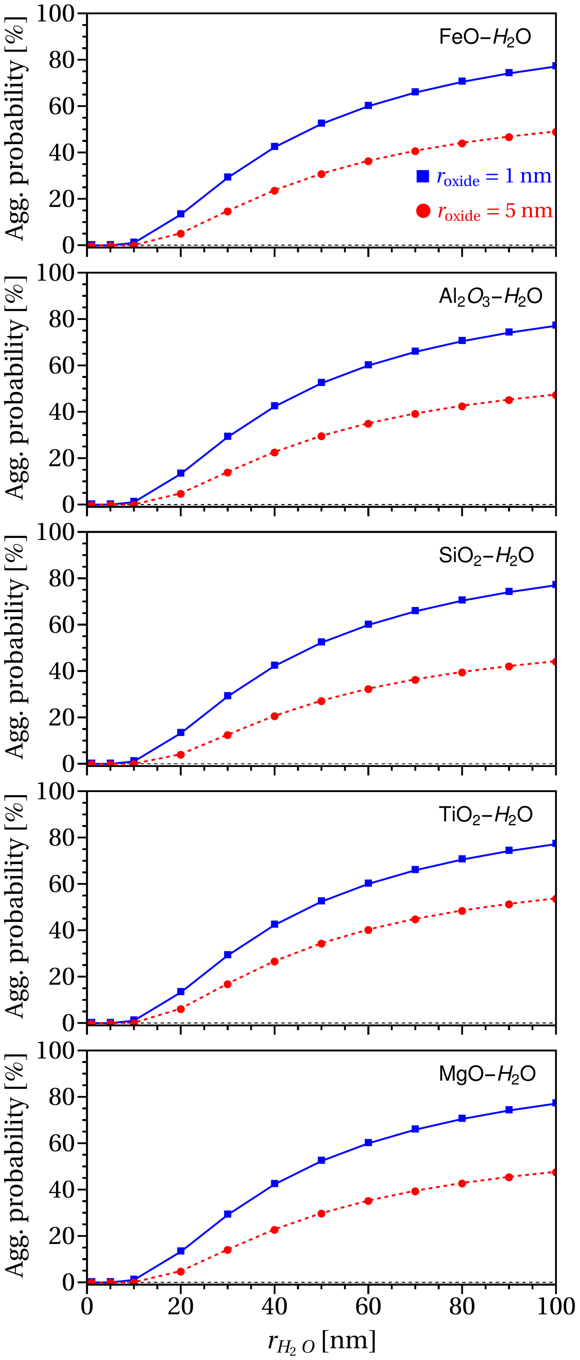

Figure 4. Aggregation probability [%] for collision between ice ($q_{H_2O} = -1e$) and different metal oxides ($q_{\text{Oxide}} = -1e$). r_{H_2O} varies from 1 to 100 nm. The solid and dashed lines are for r_{Oxide} = 1 nm (blue) and 5 nm (red), respectively. The colors are explained in the uppermost panel.

https://doi.org/10.5194/egusphere-2026-2931
Preprint. Discussion started: 4 June 2026

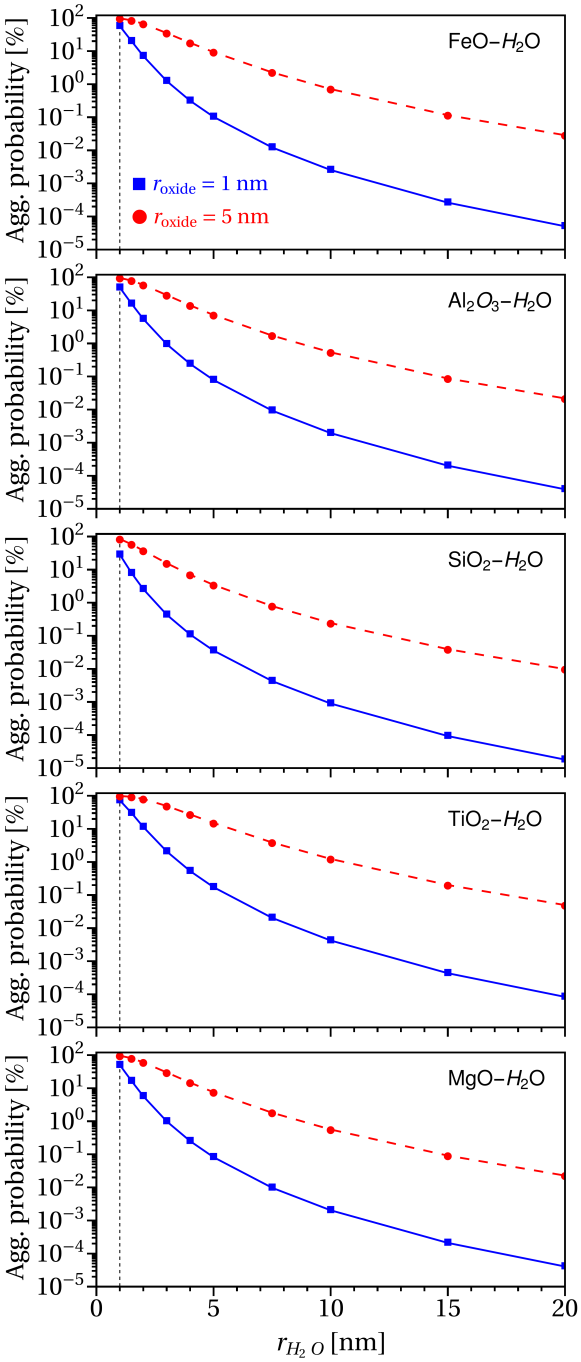

Figure 5. Aggregation probability [%] for collision between ice ($q_{H_2O} = -1e$) and different neutral metal oxides ($q_{\mathrm{Oxide}} = 0$). r_{H_2O} varies from 1 to 20 nm. The solid and dashed lines are for $r_{\mathrm{Oxide}} = 1$ nm (blue) and 5 nm (red), respectively. The colors are explained in the uppermost panel.

4 Discussion

The present study investigates the electrostatic interaction between charged ice and anthropogenic smoke particles (ASPs) in the MLT region. This estimation is essential for evaluating the outcomes of collisions and subsequent aggregation of ice and ASPs. Like-charged ice and ASPs feel strong Coulomb repulsion at large separations. Additionally, at small separations, they feel a strong attraction due to the induced polarization of the particle's surface charge. Hence, the electrostatic interaction between ice and ASPs offers important insights into the minimum (to overcome the Coulomb barrier) and maximum (to form a stable aggregate after contact) relative velocities necessary for the formation of stable aggregates. For ice and ASPs in thermal motion at $T = 150$ K, aggregation depends on particle size, mass density, and dielectric constant. In the case of a like-charged ice-ASP collision, the velocity range for growth varies from several tens of meters per second to a few meters per second. For ice particles of $r_{H_2O} \lesssim 55$ nm, the high-energy tail of the Maxwellian distribution leads to the formation of stable aggregates. For larger particles, a significant fraction near the Maxwellian peak can actively contribute to collision and aggregation. As a result, for like-charged ice-ASP, the collision aggregation probability increases with increasing r_{H_2O}. On the contrary, the present study found that in a charged-neutral ice-ASP collision, the aggregation probability reduces to approximately four to seven orders of magnitude with increasing r_{H_2O} to 20 nm. Larger ice particles have a low surface charge density, which prevents them from creating a sufficient polarization effect at short distances from neutral ASPs. Consequently, these particles tend to move apart after a collision, leading to aggregation primarily involving the lower part of the Maxwellian distribution. However, very small ice particles (a few nm) have a higher surface charge density because of their smaller surface area. This increased charge density can generate significant binding energy, allowing them to form stable aggregates when their relative collision velocity is comparable to the thermal velocity, u_{th}. For charged-neutral ice-ASP collision, the maximum velocity ranges from a few tens of m s^{-1} for $r_{H_2O} < 5$ nm to a few times 0.1 m s^{-1} for $r_{H_2O} \geq 5$ nm. Therefore, the present study suggests that like-charged ice-ASP collisions are more favorable to form stable aggregates than charged-neutral ice-ASP collisions for larger ice particles.

The aggregation of ice and ASPs has significant implications for the formation of polar mesospheric clouds. These phenomena are of considerable interest as they serve as indicators of climate change. Therefore, understanding the composition, origin, and evolution of ASPs is essential for comprehending these processes. Natural influx from meteoric ablation is believed to be the dominant source of meteoric smoke particles (MSPs). However, a significant increase in atmospheric re-entry of space debris may enhance the presence of ASPs. As a result, ASPs enriched in specific elemental species (such as Al_2O_3 and TiO_2) may exceed the abundance of their naturally occurring MSPs.

The present study suggests that for like-charged ice-ASP aggregation, there are no significant differences in the aggregation probability across different ice-oxide combinations. Therefore, particle growth will depend on the concentration of specific elemental species in the ASPs. In contrast, for the charged-neutral ice-ASP collision, the probability of ice-TiO_2 aggregation is observed to be higher due to the large dielectric constant of TiO_2, which creates a stronger polarization effect. Schulz et al. (2026) predicted that the post-ablation annual elemental mass injection of anthropogenic elements (especially Al and Ti) is going to be dominated over the natural meteoric injection in the near future. We suggest that Al_2O_3 (due to its greater abundance) and TiO_2 (due to its higher dielectric constant), both originating from anthropogenic sources, may dominate in the formation of ice-ASP aggregates. In the near future, based on the prediction of Schulz et al. (2026), we may expect a higher concentration of Al and Ti in the in-situ detected ASPs. The findings of this study are useful for future work on the impact of human space activities in the MLT region. Additionally, these results could be significant for sounding rocket experiments focused on detecting remnants of space debris in the MLT region.

Author contributions. TS and IM conceptualized the study. TS implemented and performed the numerical analysis. All authors contributed to the analysis, discussion, writing, and editing of the manuscript and approved the final version for submission.

Competing interests. The authors declare that they have no known competing financial interests or personal relationships that could have appeared to influence the work reported in this paper.

Acknowledgements. IM's Research at UiT was supported by the Research Council of Norway through grant number NFR 275503. TS and SKM acknowledge the support from the Department of Space, Government of India. TS is thankful to Prof. Elena Besley and Mr. Cameron Reeve for their suggestions regarding the calculation of electrostatic interaction energy.

References

Baptiste, J., Williamson, C., Fox, J., Stace, A. J., Hassan, M., Braun, S., Stamm, B., Mann, I., and Besley, E.: The influence of surface charge on the coalescence of ice and dust particles in the mesosphere and lower thermosphere, Atmospheric Chemistry and Physics, 21, 8735–8745, 2021.

Bardeen, C., Toon, O., Jensen, E., Marsh, D., and Harvey, V.: Numerical simulations of the three-dimensional distribution of meteoric dust in the mesosphere and upper stratosphere, Journal of Geophysical Research: Atmospheres, 113, 2008.

Baumann, C., Rapp, M., Kero, A., and Enell, C.-F.: Meteor smoke influences on the D-region charge balance–review of recent in situ measurements and one-dimensional model results, Annales Geophysicae, 31, 2049–2062, 2013.

Baumann, C., Rapp, M., Anttila, M., Kero, A., and Verronen, P. T.: Effects of meteoric smoke particles on the D region ion chemistry, Journal of Geophysical Research: Space Physics, 120, 10–823, 2015.

Bichoutskaia, E., Boatwright, A. L., Khachatourian, A., and Stace, A. J.: Electrostatic analysis of the interactions between charged particles of dielectric materials, The Journal of chemical physics, 133, 2010.

Brazil Lindgren, E.: Theoretical analysis of the electrostatic interactions between charged polarisable particles, Ph.D. thesis, University of Nottingham, 2017.

Gunnarsdottir, T. L., Mann, I., Feng, W., Huyghebaert, D. R., Haeggstroem, I., Ogawa, Y., Saito, N., Nozawa, S., and Kawahara, T. D.: Influence of meteoric smoke particles on the incoherent scatter measured with EISCAT VHF, Annales Geophysicae, 42, 213–228, 2024.

Havnes, O., Aslaksen, T., and Brattli, A.: Charged dust in the Earth's middle atmosphere, Physica Scripta, 2001, 133–137, 2001.

Howard, K. and Ah, A.: Large constellations of satellites: Mitigating environmental and other effects, United States Government Accountability Office, Washington, DC, Tech. Rep. GAO-22–105166, 2022.

Latteck, R., Renkwitz, T., and Chau, J. L.: Two decades of long-term observations of polar mesospheric echoes at 69 N, Journal of Atmospheric and Solar-Terrestrial Physics, 216, 105 576, 2021.

Lübken, F.-J., Baumgarten, G., and Berger, U.: Long term trends of mesopheric ice layers: A model study, Journal of atmospheric and solar-terrestrial physics, 214, 105 378, 2021.

Mann, I., Meyer-Vernet, N., and Czechowski, A.: Dust in the planetary system: Dust interactions in space plasmas of the solar system, Physics reports, 536, 1–39, 2014.

Mann, I., Gunnarsdottir, T., Häggström, I., Eren, S., Tjulin, A., Myrvang, M., Rietveld, M., Dalin, P., Jozwicki, D., and Trollvik, H.: Radar studies of ionospheric dusty plasma phenomena, Contributions to Plasma Physics, 59, e201900 005, 2019.

Megner, L., Siskind, D., Rapp, M., and Gumbel, J.: Global and temporal distribution of meteoric smoke: A two-dimensional simulation study, Journal of Geophysical Research: Atmospheres, 113, 2008.

Misra, S., Mishra, S., and Sodha, M.: Charge Distribution in Mesospheric Clouds, in: Dusty/complex Plasmas: Basic and Interdisciplinary Research: Sixth International Conference on the Physics of Dusty Plasmas, vol. 1397, pp. 417–418, 2011.

Murphy, D. M., Abou-Ghanem, M., Cziczo, D. J., Froyd, K. D., Jacquot, J., Lawler, M. J., Maloney, C., Plane, J. M., Ross, M. N., Schill, G. P., et al.: Metals from spacecraft reentry in stratospheric aerosol particles, Proceedings of the National Academy of Sciences, 120, e2313374 120, 2023.

Plane, J. M.: Atmospheric chemistry of meteoric metals, Chemical reviews, 103, 4963–4984, 2003.

Plane, J. M., Feng, W., and Dawkins, E. C.: The mesosphere and metals: Chemistry and changes, Chemical reviews, 115, 4497–4541, 2015.

Rapp, M. and Thomas, G. E.: Modeling the microphysics of mesospheric ice particles: Assessment of current capabilities and basic sensitivities, Journal of Atmospheric and Solar-Terrestrial Physics, 68, 715–744, 2006.

Schulz, L. and Glassmeier, K.-H.: On the anthropogenic and natural injection of matter into Earth's atmosphere, Advances in Space Research, 67, 1002–1025, 2021.

Schulz, L., Glassmeier, K.-H., Herberhold, M., Mitchell, A., Murphy, D. M., Plane, J. M., and Plaschke, F.: Space waste: An update of the anthropogenic matter injection into Earth's atmosphere, Advances in Space Research, 77, 9589–9616, https://doi.org/https://doi.org/10.1016/j.asr.2026.03.026, 2026.

Sodha, M., Misra, S., Mishra, S., and Dixit, A.: Kinetics of polar mesospheric plasma layers: Comparison of theoretical results with observations, Physics of Plasmas, 18, 2011.

Tanaka, K. K., Mann, I., and Kimura, Y.: Formation of ice particles through nucleation in the mesosphere, Atmospheric chemistry and physics, 22, 5639–5650, 2022.

https://doi.org/10.5194/egusphere-2026-2931
Preprint. Discussion started: 4 June 2026

Appendix A: Detail tabulated results of like-charged ice-ASP collisions

E_{Coul}, E_0, u_{min}, u_{max}, and the percentage of aggregation values for ice-ASP collisions for different oxides. The relevant dielectric constants and mass density values are taken from Table 1. Other parameters used: $q_{H_2O} = q_{\text{Oxide}} = -1e$, $T = 150$ K, and $k_r = 0.9$.

$r_{\text{FeO}} = 1$ nm					
r_{H_2O} (nm)	E_{Coul} (eV)	E_0 (eV)	u_{min} m s^{-1}	u_{max} m s^{-1}	Agg(%)
1	0.6423	0.6423	248.7598	248.7598	0.0000
5	0.1447	-0.0545	44.9713	51.7234	0.0053
10	0.0724	-0.2338	31.1315	43.9439	1.0698
20	0.0362	-0.3352	21.9535	40.5233	13.2876
30	0.0241	-0.3705	17.9199	39.4119	29.1812
40	0.0181	-0.3879	15.5179	38.8381	42.3481
50	0.0145	-0.3978	13.8792	38.4665	52.3978
60	0.0121	-0.4037	12.6697	38.1890	60.0286
70	0.0103	-0.4072	11.7296	37.9615	65.9031
80	0.0090	-0.4092	10.9719	37.7627	70.5071
90	0.0080	-0.4101	10.3443	37.5816	74.1801
100	0.0072	-0.4102	9.8134	37.4118	77.1587

$r_{\text{FeO}} = 5$ nm					
r_{H_2O} (nm)	E_{Coul} (eV)	E_0 (eV)	u_{min} m s^{-1}	u_{max} m s^{-1}	Agg(%)
1	0.1502	-0.0148	111.7681	125.3414	0.0034
5	0.1285	0.1285	9.9652	9.9652	0.0000
10	0.0722	0.0663	3.6980	3.7331	0.1024
20	0.0362	0.0047	2.0562	2.2565	5.2363
30	0.0241	-0.0225	1.6256	1.9597	14.8717
40	0.0181	-0.0375	1.3963	1.8320	23.8121
50	0.0145	-0.0471	1.2452	1.7599	30.9591
60	0.0121	-0.0537	1.1352	1.7135	36.5066
70	0.0103	-0.0585	1.0503	1.6809	40.8240
80	0.0090	-0.0621	0.9821	1.6568	44.2250
90	0.0080	-0.0650	0.9257	1.6382	46.9430
100	0.0072	-0.0674	0.8781	1.6235	49.1463

$r_{\mathrm{Al_2O_3}} = 1$ nm					
r_{H_2O} (nm)	E_{Coul} (eV)	E_0 (eV)	u_{min} m s^{-1}	u_{max} m s^{-1}	Agg(%)
1	0.6445	0.6445	259.9699	259.9699	0.0000
5	0.1447	-0.0394	57.0547	65.0123	0.0052
10	0.0724	-0.2158	39.8196	55.3755	1.0677
20	0.0362	-0.3163	28.1099	50.9490	13.2774
30	0.0241	-0.3518	22.9476	49.5124	29.1648
40	0.0181	-0.3697	19.8723	48.7888	42.3278
50	0.0145	-0.3802	17.7739	48.3377	52.3750
60	0.0121	-0.3868	16.2250	48.0151	60.0043
70	0.0103	-0.3911	15.0212	47.7605	65.8777
80	0.0090	-0.3939	14.0509	47.5447	70.4811
90	0.0080	-0.3956	13.2472	47.3521	74.1538
100	0.0072	-0.3966	12.5673	47.1735	77.1322

$r_{\mathrm{Al_2O_3}} = 5$ nm					
r_{H_2O} (nm)	E_{Coul} (eV)	E_0 (eV)	u_{min} m s^{-1}	u_{max} m s^{-1}	Agg(%)
1	0.1538	0.0211	113.1416	124.0604	0.0025
5	0.1289	0.1289	10.4233	10.4233	0.0000
10	0.0722	0.0673	4.3124	4.3463	0.0853
20	0.0362	0.0074	2.5871	2.8181	4.8735
30	0.0241	-0.0192	2.0703	2.4677	14.1033
40	0.0181	-0.0339	1.7839	2.3086	22.7568
50	0.0145	-0.0434	1.5927	2.2169	29.7084
60	0.0121	-0.0499	1.4528	2.1570	35.1185
70	0.0103	-0.0546	1.3444	2.1148	39.3356
80	0.0090	-0.0583	1.2573	2.0835	42.6608
90	0.0080	-0.0611	1.1852	2.0593	45.3199
100	0.0072	-0.0635	1.1243	2.0400	47.4762

$r_{\mathrm{SiO_2}} = 1$ nm					
r_{H_2O} (nm)	E_{Coul} (eV)	E_0 (eV)	u_{min} m s^{-1}	u_{max} m s^{-1}	Agg(%)
1	0.6501	0.6501	269.6650	269.6650	0.0000
5	0.1447	-0.0124	65.3341	73.1839	0.0051
10	0.0724	-0.1832	45.7412	61.8524	1.0618
20	0.0362	-0.2822	32.3032	56.5449	13.2480
30	0.0241	-0.3176	26.3719	54.8287	29.1172
40	0.0181	-0.3357	22.8378	53.9810	42.2680
50	0.0145	-0.3467	20.4264	53.4732	52.3073
60	0.0121	-0.3540	18.6464	53.1311	59.9311
70	0.0103	-0.3591	17.2630	52.8803	65.8010
80	0.0090	-0.3628	16.1479	52.6836	70.4021
90	0.0080	-0.3656	15.2242	52.5202	74.0734
100	0.0072	-0.3676	14.4428	52.3776	77.0511

$r_{\mathrm{SiO_2}} = 5$ nm					
r_{H_2O} (nm)	E_{Coul} (eV)	E_0 (eV)	u_{min} m s^{-1}	u_{max} m s^{-1}	Agg(%)
1	0.1662	0.1013	117.6359	122.9040	0.0008
5	0.1316	0.1300	10.8504	10.8649	0.0004
10	0.0722	0.0691	4.7597	4.7841	0.0561
20	0.0362	0.0122	2.9529	3.1740	4.2001
30	0.0241	-0.0132	2.3743	2.7723	12.6509
40	0.0181	-0.0276	2.0483	2.5846	20.7493
50	0.0145	-0.0368	1.8296	2.4752	27.3228
60	0.0121	-0.0431	1.6691	2.4034	32.4677
70	0.0103	-0.0478	1.5448	2.3528	36.4918
80	0.0090	-0.0514	1.4448	2.3152	39.6715
90	0.0080	-0.0542	1.3620	2.2861	42.2176
100	0.0072	-0.0565	1.2920	2.2630	44.2841

$r_{\mathrm{TiO_2}} = 1$ nm					
r_{H_2O} (nm)	E_{Coul} (eV)	E_0 (eV)	u_{min} m s^{-1}	u_{max} m s^{-1}	Agg(%)
1	0.6381	0.6381	253.8786	253.8786	0.0000
5	0.1447	-0.0993	51.9398	61.3571	0.0054
10	0.0724	-0.2873	36.1503	53.2014	1.0732
20	0.0362	-0.3911	25.5106	49.5316	13.3040
30	0.0241	-0.4267	20.8250	48.3192	29.2081
40	0.0181	-0.4439	18.0339	47.6796	42.3823
50	0.0145	-0.4534	16.1296	47.2559	52.4378
60	0.0121	-0.4590	14.7240	46.9347	60.0733
70	0.0103	-0.4622	13.6316	46.6702	65.9520
80	0.0090	-0.4639	12.7510	46.4405	70.5601
90	0.0080	-0.4646	12.0216	46.2339	74.2371
100	0.0072	-0.4647	11.4046	46.0438	77.2198

$r_{\mathrm{TiO_2}} = 5$ nm					
r_{H_2O} (nm)	E_{Coul} (eV)	E_0 (eV)	u_{min} m s^{-1}	u_{max} m s^{-1}	Agg(%)
1	0.1448	-0.0959	109.7412	129.3803	0.0054
5	0.1277	0.1277	10.1917	10.1917	0.0000
10	0.0721	0.0629	4.0450	4.1056	0.1575
20	0.0362	-0.0041	2.3618	2.6525	6.2985
30	0.0241	-0.0331	1.8823	2.3481	17.0682
40	0.0181	-0.0489	1.6202	2.2146	26.8028
50	0.0145	-0.0588	1.4460	2.1385	34.4904
60	0.0121	-0.0656	1.3187	2.0891	40.4172
70	0.0103	-0.0705	1.2203	2.0542	45.0100
80	0.0090	-0.0742	1.1411	2.0282	48.6166
90	0.0080	-0.0771	1.0757	2.0081	51.4910
100	0.0072	-0.0795	1.0203	1.9919	53.8150

$r_{\mathrm{MgO}} = 1$ nm					
r_{H_2O} (nm)	E_{Coul} (eV)	E_0 (eV)	u_{min} m s^{-1}	u_{max} m s^{-1}	Agg(%)
1	0.6441	0.6441	259.2941	259.2941	0.0000
5	0.1447	-0.0415	56.4326	64.3901	0.0052
10	0.0724	-0.2184	39.3738	54.8745	1.0680
20	0.0362	-0.3190	27.7942	50.5113	13.2790
30	0.0241	-0.3545	22.6898	49.0942	29.1675
40	0.0181	-0.3723	19.6490	48.3782	42.3312
50	0.0145	-0.3828	17.5742	47.9296	52.3788
60	0.0121	-0.3893	16.0427	47.6068	60.0083
70	0.0103	-0.3935	14.8524	47.3506	65.8819
80	0.0090	-0.3962	13.8930	47.1322	70.4854
90	0.0080	-0.3978	13.0983	46.9365	74.1582
100	0.0072	-0.3986	12.4261	46.7546	77.1366

$r_{\mathrm{MgO}} = 5$ nm					
r_{H_2O} (nm)	E_{Coul} (eV)	E_0 (eV)	u_{min} m s^{-1}	u_{max} m s^{-1}	Agg(%)
1	0.1532	0.0157	112.9156	124.2325	0.0026
5	0.1289	0.1289	10.3945	10.3945	0.0000
10	0.0722	0.0672	4.2795	4.3142	0.0877
20	0.0362	0.0070	2.5597	2.7912	4.9259
30	0.0241	-0.0196	2.0474	2.4445	14.2150
40	0.0181	-0.0345	1.7640	2.2874	22.9105
50	0.0145	-0.0439	1.5749	2.1969	29.8908
60	0.0121	-0.0504	1.4365	2.1379	35.3209
70	0.0103	-0.0552	1.3294	2.0963	39.5527
80	0.0090	-0.0588	1.2432	2.0654	42.8890
90	0.0080	-0.0617	1.1719	2.0416	45.5567
100	0.0072	-0.0640	1.1117	2.0226	47.7200

Appendix B: Detail tabulated results of charged-neutral ice-ASP collisions

E_{Coul}, E_0, u_{min}, u_{max}, and the percentage of aggregation values for ice-ASP collisions for different oxides. The relevant dielectric constants and mass density values are taken from Table 1. Other parameters used: $q_{H_2O} = -1e$, $q_{\text{Oxide}} = 0$, $T = 150$ K, and $k_r = 0.9$.

$r_{\text{FeO}} = 1$ nm					
r_{H_2O} (nm)	E_{Coul} (eV)	E_0 (eV)	u_{min} m s^{-1}	u_{max} m s^{-1}	Agg(%)
1	0	-0.07594215	0	41.42797192	56.88367944
1.5	0	-0.02767035	0	15.68680281	19.95644263
2	0	-0.01249221	0	8.33154154	7.09087004
3	0	-0.00367904	0	3.76027350	1.24531246
4	0	-0.00145103	0	2.22969925	0.31597967
5	0	-0.00068381	0	1.49711227	0.10307867
7.5	0	-0.00016461	0	0.72214555	0.01224326
10	0	-0.00005779	0	0.42607981	0.00254984
15	0	-0.00001271	0	0.19938935	0.00026315
20	0	-0.00000425	0	0.11522100	0.00005087

$r_{\text{FeO}} = 5$ nm					
r_{H_2O} (nm)	E_{Coul} (eV)	E_0 (eV)	u_{min} m s^{-1}	u_{max} m s^{-1}	Agg(%)
1	0	-0.26778015	0	72.26674688	97.88024662
1.5	0	-0.15004748	0	29.49077690	85.77882537
2	0	-0.09473403	0	15.26494270	67.07380653
3	0	-0.04557675	0	5.83245386	35.24975139
4	0	-0.02530380	0	2.88668998	17.88114770
5	0	-0.01534226	0	1.66548962	9.36488041
7.5	0	-0.00557969	0	0.63005319	2.27875730
10	0	-0.00251636	0	0.33445444	0.71333298
15	0	-0.00074021	0	0.15086028	0.11601937
20	0	-0.00029176	0	0.08942654	0.02885039

https://doi.org/10.5194/egusphere-2026-2931
Preprint. Discussion started: 4 June 2026

$r_{\mathrm{Al_2O_3}} = 1$ nm					
r_{H_2O} (nm)	E_{Coul} (eV)	E_0 (eV)	$u_{\min}$ m s^{-1}	$u_{\max}$ m s^{-1}	Agg(%)
1	0	-0.06330082	0	39.45961588	48.65964667
1.5	0	-0.02299548	0	15.82551315	15.86466799
2	0	-0.01037888	0	8.85486907	5.49176598
3	0	-0.00306081	0	4.22837430	0.95133035
4	0	-0.00120911	0	2.56096110	0.24098255
5	0	-0.00057056	0	1.73497605	0.07866000
7.5	0	-0.00013766	0	0.84331165	0.00936621
10	0	-0.00004840	0	0.49874202	0.00195445
15	0	-0.00001066	0	0.23378085	0.00020218
20	0	-0.00000357	0	0.13518419	0.00003913

$r_{\mathrm{Al_2O_3}} = 5$ nm					
r_{H_2O} (nm)	E_{Coul} (eV)	E_0 (eV)	$u_{\min}$ m s^{-1}	$u_{\max}$ m s^{-1}	Agg(%)
1	0	-0.22987472	0	66.98426860	96.04389737
1.5	0	-0.12759959	0	27.23293762	79.87600958
2	0	-0.08001931	0	14.07492611	59.29591781
3	0	-0.03816322	0	5.39390656	29.06784819
4	0	-0.02108362	0	2.69818508	14.20686985
5	0	-0.01274786	0	1.58384176	7.28988493
7.5	0	-0.00462459	0	0.63477234	1.73722727
10	0	-0.00208567	0	0.35503769	0.54078703
15	0	-0.00061456	0	0.16946542	0.08788861
20	0	-0.00024266	0	0.10261572	0.02189488

$r_{\mathrm{SiO_2}} = 1$ nm					
r_{H_2O} (nm)	E_{Coul} (eV)	E_0 (eV)	u_{min} m s^{-1}	u_{max} m s^{-1}	Agg(%)
1	0	-0.03731667	0	31.29202590	28.34513821
1.5	0	-0.01347942	0	12.99778768	7.86520505
2	0	-0.00608175	0	7.47884257	2.57918406
3	0	-0.00179882	0	3.66900005	0.43450102
4	0	-0.00071294	0	2.24454265	0.10969937
5	0	-0.00033735	0	1.52767475	0.03585282
7.5	0	-0.00008178	0	0.74619765	0.00429148
10	0	-0.00002884	0	0.44223747	0.00089913
15	0	-0.00000638	0	0.20772245	0.00009348
20	0	-0.00000214	0	0.12024451	0.00001815

$r_{\mathrm{SiO_2}} = 5$ nm					
r_{H_2O} (nm)	E_{Coul} (eV)	E_0 (eV)	u_{min} m s^{-1}	u_{max} m s^{-1}	Agg(%)
1	0	-0.14481751	0	53.18435026	84.57081081
1.5	0	-0.07872104	0	21.41438244	58.54029135
2	0	-0.04865465	0	11.00424354	37.72658280
3	0	-0.02278349	0	4.20340502	15.68017381
4	0	-0.01245966	0	2.11329906	7.06561462
5	0	-0.00749072	0	1.25397552	3.47266274
7.5	0	-0.00270356	0	0.52065134	0.79279030
10	0	-0.00121926	0	0.29951084	0.24399460
15	0	-0.00036044	0	0.14689812	0.03958601
20	0	-0.00014282	0	0.08985411	0.00989670

$r_{\mathrm{TiO_2}} = 1$ nm					
r_{H_2O} (nm)	E_{Coul} (eV)	E_0 (eV)	u_{min} m s^{-1}	u_{max} m s^{-1}	Agg(%)
1	0	-0.10748237	0	50.46502358	72.72521962
1.5	0	-0.03953333	0	19.87068131	30.23094596
2	0	-0.01787784	0	10.90448837	11.47041056
3	0	-0.00525197	0	5.09245862	2.08831748
4	0	-0.00206398	0	3.05461675	0.53249738
5	0	-0.00096964	0	2.05900229	0.17351332
7.5	0	-0.00023215	0	0.99475814	0.02048996
10	0	-0.00008123	0	0.58657321	0.00424776
15	0	-0.00001780	0	0.27412007	0.00043594
20	0	-0.00000594	0	0.15824600	0.00008398

$r_{\mathrm{TiO_2}} = 5$ nm					
r_{H_2O} (nm)	E_{Coul} (eV)	E_0 (eV)	u_{min} m s^{-1}	u_{max} m s^{-1}	Agg(%)
1	0	-0.35560100	0	83.29675421	99.51300247
1.5	0	-0.20408700	0	34.41970968	93.98301309
2	0	-0.13114600	0	17.99251268	80.94056878
3	0	-0.06458872	0	6.98378075	49.54957859
4	0	-0.03634800	0	3.50546588	27.51463309
5	0	-0.02221110	0	2.05187900	15.18278301
7.5	0	-0.00813572	0	0.80625787	3.90367138
10	0	-0.00366938	0	0.44186457	1.24053969
15	0	-0.00107452	0	0.20602418	0.20218091
20	0	-0.00042151	0	0.12346793	0.05002817

$r_{\text{MgO}} = 1$ nm					
r_{H_2O} (nm)	E_{Coul} (eV)	E_0 (eV)	u_{min} m s^{-1}	u_{max} m s^{-1}	Agg(%)
1	0	-0.06518563	0	39.94953690	49.95803091
1.5	0	-0.02369040	0	15.97826451	16.47040590
2	0	-0.01069289	0	8.91950404	5.72371570
3	0	-0.00315276	0	4.24918170	0.99353120
4	0	-0.00124514	0	2.57127964	0.25173429
5	0	-0.00058745	0	1.74126524	0.08216208
7.5	0	-0.00014169	0	0.84602386	0.00977953
10	0	-0.00004980	0	0.50026372	0.00204010
15	0	-0.00001097	0	0.23445830	0.00021097
20	0	-0.00000367	0	0.13556562	0.00004083

$r_{\text{MgO}} = 5$ nm					
r_{H_2O} (nm)	E_{Coul} (eV)	E_0 (eV)	u_{min} m s^{-1}	u_{max} m s^{-1}	Agg(%)
1	0	-0.23565386	0	67.81945757	96.40095369
1.5	0	-0.13099421	0	27.59063615	80.89601887
2	0	-0.08223149	0	14.26551627	60.55685789
3	0	-0.03926936	0	5.46823176	30.00751117
4	0	-0.02171061	0	2.73437990	14.74891163
5	0	-0.01313239	0	1.60380908	7.59124317
7.5	0	-0.00476585	0	0.64100071	1.81466679
10	0	-0.00214937	0	0.35767946	0.56536184
15	0	-0.00063317	0	0.17031988	0.09189325
20	0	-0.00024995	0	0.10304051	0.02288643